Annals of Biomedical Engineering, Vol. 44, No. 9, September 2016 (© 2016) pp. 2661–2673
DOI: 10.1007/s10439-016-1574-x

Parametric Modeling of the Mouse Left Ventricular Myocardial Fiber Structure

SAMER S. MERCHANT,[1] ARNOLD DAVID GOMEZ,[1,2] JAMES L. MORGAN,[1] and EDWARD W. HSU[1]

[1]Department of Bioengineering, University of Utah, 36 S Wasatch Dr Rm 3100, Salt Lake City, UT 84112, USA; and [2]Division of Cardiothoracic Surgery, University of Utah, Salt Lake City, UT, USA

(*Received 1 October 2015; accepted 17 February 2016; published online 4 March 2016*)

Associate Editor Joel D. Stitzel oversaw the review of this article.

Abstract—Magnetic resonance diffusion tensor imaging (DTI) has greatly facilitated detailed quantifications of myocardial structures. However, structural patterns, such as the distinctive transmural rotation of the fibers, remain incompletely described. To investigate the validity and practicality of pattern-based analysis, 3D DTI was performed on 13 fixed mouse hearts and fiber angles in the left ventricle were transformed and fitted to parametric expressions constructed from elementary functions of the prolate spheroidal spatial variables. It was found that, on average, the myocardial fiber helix angle could be represented to 6.5° accuracy by the equivalence of a product of 10th-order polynomials of the radial and longitudinal variables, and 17th-order Fourier series of the circumferential variable. Similarly, the fiber imbrication angle could be described by 10th-order polynomials and 24th-order Fourier series, to 5.6° accuracy. The representations, while relatively concise, did not adversely affect the information commonly derived from DTI datasets including the whole-ventricle mean fiber helix angle transmural span and atlases constructed for the group. The unique ability of parametric models for predicting the 3D myocardial fiber structure from finite number of 2D slices was also demonstrated. These findings strongly support the principle of parametric modeling for characterizing myocardial structures in the mouse and beyond.

Keywords—DTI, Cardiac, Parametric modelling, Cardiac fiber architecture prediction, Cardiac DTI atlas.

INTRODUCTION

Functions of the heart depend heavily on the underlying myocardial structure and its spatial organization. For example, electrical propagation is three times faster along than across the myocardial fiber direction.[23] Ventricular torsion during contraction arises from the helical arrangement of the myocardial fiber orientation.[4,8] Moreover, alterations in the cardiac environment such as elevated afterload due to hypertension [7,13] and diseases like hypertrophic cardiomyopathy[33] are known to cause myocardial remodeling at both microscopic and macroscopic levels. For these reasons, quantitative characterization of the myocardial structure is useful to better understand the normal cardiac physiology, and as means for detecting, diagnosing and monitoring cardiac diseases.

Magnetic resonance diffusion tensor imaging (DTI)[5] has emerged as the tool-of-choice to non-invasively quantify the 3D myocardial structure of the heart. The primary DTI eigenvector (i.e., the direction in which diffusion is the fastest) has been directly correlated to the fiber orientation of the freshly excised,[21] perfused,[36] and fixed[19] myocardium. Additionally, the secondary DTI eigenvector has been associated with the myocardial laminar or sheet structure.[34] DTI has been used to study hearts in various species including human,[32,34] large[44] and small[10,22] animals. Because of its sensitivity to tissue microstructural remodeling, DTI changes have been reported cardiac pathologies such as infarct,[25,41] hypertrophy,[15,35] and heart failure.[18]

Analyzes of myocardial DTI data have included comparison of DTI-derived scalar quantities such as the mean diffusivity and fractional anisotropy,[1] and directional parameters.[42] Computation of the directional quantities is more challenging, since they are referenced to the local cardiac morphology. For example, the commonly reported fiber helix angle is the inclination from the circumferential axis of the primary DTI eigenvector projected onto the epicardial tangential plane. Advances in computational anatomy have allowed DTI datasets of same organs from dif-

Address correspondence to Samer S. Merchant, Department of Bioengineering, University of Utah, 36 S Wasatch Dr Rm 3100, Salt Lake City, UT 84112, USA. Electronic mail: samer.merchant@gmail.com

0090-6964/16/0900-2661/0 © 2016 Biomedical Engineering Society

ferent subjects to be registered,[29,43] transformed,[2] and described in a standardized coordinate system on a voxel-by-voxel basis, which in turn made construction of numerical models representing structural averages, or atlases, of organs including the heart[27,30] possible. Besides challenges associated with handling relatively large datasets, voxel-based analyzes commonly assume that the measured quantities in the voxels behave independently, which neglects any structural pattern that may be present in the organ.

The existence of myocardial structural patterns, epitomized by the smoothly-varying double helical arrangement of ventricular myocardial fibers, is long known.[37] Instead of helix angles in all voxels, their transmural slope of change, or span, has been used as a single metric for measuring the myocardial fiber structure in studying, for example, hearts among different species[17] and hypertrophied hearts.[33] These basic myocardial structural patterns have been incorporate into rule-based predictions of fiber orientation for generating computational models of the heart.[6] Moreover, fitting the helix angle profile to a higher-order polynomial function of the transmural distance was found to improve the accuracy of the computational modeling.[14] Despite the ability to quantify myocardial structures in whole hearts *via* DTI and clear benefits of pattern-based descriptions, myocardial structural patterns in 3D remain to be investigated systematically.

The goals of the current study are therefore to determine the feasibility of representing the myocardial fiber structure as parameterized functions of the 3D spatial variables, and explore its potential utility for capturing the essential fiber structural information, constructing group atlases, and performing subject-specific predictions of the fiber structure. Being a first study of its kind, the main focus is on evaluating the general validity of the parametric approach for modeling the 3D myocardial fiber architecture, and not on optimization of the specific computational procedures involved. Although based on DTI datasets obtained from fixed mouse hearts, the methodologies developed and conclusions reached in the current study are expected to be applicable to hearts from other species prepared using alternative means or imaged *in vivo*.

METHODS

Specimen Preparation and Image Acquisition

Using protocols approved by the University of Utah Institutional Animal Care and Use Committee, hearts ($n = 13$) were excised from isoflurane-anesthetized 3 month-old male C57B/L6 mice, rapidly cannulated *via* the aorta, and arrested by retrograde perfusion of KCl, with a small amount of alginate (Accu-Cast, Bend, Oregon) injected into the left ventricle (LV) to maintain its end-diastolic morphology. Subsequently, the hearts were immersion fixed in 10% formalin for a minimum of 48 h. In preparation for imaging, each specimen was placed in a 0.8 cm-diameter sealed tube filled with Fomblin (Solvay Solexis, West Deptford, NJ).

Diffusion tensor imaging was performed using a 1.0 cm-diameter loop-gap radiofrequency transmitter–receiver and standard 3D spin-echo echo-planar scans (100 μm isotropic resolution, 4-shot acquisition, $100 \times 63 \times 100$ matrix size, TE/TR = 25/500 ms) on a Bruker Biospec 70/30 instrument (Bruker Biospin, Ettlingen, Germany). Each DTI dataset consisted of 192 images encoded pairwise (both positive and negative senses) with diffusion-weighting b-value of 1000 s/mm^2 in 96 directions plus 4 non-weighted (b-value of zero, or $b0$) images. Intensities from image pairs were geometrically averaged to correct for effects of gradient cross-terms.[20] Using a combination of routines written in MATLAB (release R2012b, MathWorks, Natick, MA) and C, diffusion tensors were estimated *via* nonlinear least squares multivariate curve fitting,[24] and decomposed into their eigenvectors and eigenvalues on a voxel-by-voxel basis. The eigenvector of the largest eigenvalue was taken to be the local myocardial fiber orientation.

Determination of Fiber orientation Quantities in Standardized Coordinates

To provide a common coordinate system for subsequent modeling analyzes, using Amira 5.4.2 (VSG, Konrad-Zuse-Zentrum Berlin) and codes written in C and MATLAB running on a custom workstation (AMD 2.4 GHz Phenom II quad-core CPU, 16 GB RAM with Parallel Computing Toolbox for Matlab), DTI images for each heart were re-oriented such that the cardiac long axis and the plane bisecting the ventricles were aligned with the z and x axes, respectively, of the imaging volume. A binary mask of the left ventricle (LV) distal to the equatorial plane was generated *via* intensity segmentation. Subsequently, using procedures adapted from a previous study[38] and detailed in the Appendix, coordinates of the LV of each specimen were represented on a normalized prolate hemispheroidal volume in terms of the spherical radial μ, circumferential ψ and azimuthal ν variables. The local tangential basis vectors of the prolate hemispheroidal volume were mapped onto the anatomical space *via* rotational transformation[2] to ensure orthogonality of the reference axes, and used for computing myocardial fiber orientation helix angle α

and imbrication (or transverse) angle α' from the primary DTI eigenvector as previously described.[22,37]

Construction of Parametric Models of Fiber Orientation Quantities

Without loss of generality, the fiber orientation quantities α and α' were modeled as products of finite-order polynomials of μ and v, and due to its periodic nature, Fourier series of ψ according to,

$$\alpha = \left(\sum_{i=0}^{n_\mu} a_i \mu^i\right)\left(\sum_{j=0}^{n_v} b_j v^j\right)\left(\sum_{k=0}^{n_\psi} c_k \cos(k\psi) + d_k \sin(k\psi)\right) \tag{1}$$

$$\alpha' = \left(\sum_{i=0}^{n'_\mu} a'_i \mu^i\right)\left(\sum_{j=0}^{n'_v} b'_j v^j\right)\left(\sum_{k=0}^{n'_\psi} c'_k \cos(k\psi) + d'_k \sin(k\psi)\right). \tag{2}$$

Instead of directly determining the coefficients in the expressions, Eqs. (1) and (2) were first linearized by expanding into the forms,

$$\begin{aligned}\alpha = {} & p_{0,0,0} + p_{1,0,0}\mu + p_{0,1,0}v + p_{0,0,1}\cos(\psi) + q_{0,0,1}\sin(\psi) \\ & + \cdots + p_{i,j,k}\mu^i v^j \cos(k\psi) + q_{i,j,k}\mu^i v^j \sin(k\psi) + \cdots \\ & + p_{n_\mu,n_\psi,n_v}\mu^{n_\mu} v^{n_v} \cos(n_\psi\psi) + q_{n_\mu,n_\psi,n_v}\mu^{n_\mu} v^{n_v} \sin(n_\psi\psi),\end{aligned} \tag{3}$$

and

$$\begin{aligned}\alpha' = {} & p'_{0,0,0} + p'_{1,0,0}\mu + p'_{0,1,0}v + p'_{0,0,1}\cos(\psi) + q'_{0,0,1}\sin(\psi) \\ & + \cdots + p'_{i,j,k}\mu^i v^j \cos(k\psi) + q'_{i,j,k}\mu^i v^j \sin(k\psi) \\ & + \cdots + p'_{n'_\mu,n'_\psi,n'_v}\mu^{n'_\mu} v^{n'_v} \cos(n'_\psi\psi) \\ & + q'_{n'_\mu,n'_\psi,n'_v}\mu^{n'_\mu} v^{n'_v} \sin(n'_\psi\psi).\end{aligned} \tag{4}$$

The coefficients of the expanded expressions were estimated from the measured fiber orientation quantities *via* linear least squares fitting by setting up Eqs. (3) and (4) for each voxel of the LV in the forms of linear systems of equations according to:

$$[\alpha] = [\mathrm{M}]\begin{bmatrix}\mathrm{P}\\ \mathrm{Q}\end{bmatrix} \tag{5}$$

$$[\alpha'] = [\mathrm{M}']\begin{bmatrix}\mathrm{P}'\\ \mathrm{Q}'\end{bmatrix}. \tag{6}$$

Equations (5) and (6) were then solved using economized singular value decomposition (SVD).[16] The rationale was that the number of voxels in the LV was an order of magnitude greater than the number of coefficients to be computed (see Table 1), which resulted the matrices M and M' to have markedly more rows than columns. Therefore, it would be sufficient to solve Eqs. (5) and (6) using economized SVD of the matrices, which was more practical computationally than full SVD.

TABLE 1. Voxel count, optimal myocardial fiber helix and imbrication angle model orders according to *F*-tests in each prolate spheroidal spatial dimensions, and corresponding number of terms in the expanded parametric expressions and fitting errors determined for individual hearts.

		Helix angle				Imbrication angle			
		Optimal order			RMSE	Optimal order			RMSE
Heart#	Voxels	μ, v	ψ	Terms	(°)	μ, v	ψ	Terms	(°)
1	24752	9	29	5900	4.4	7	46	5952	4.7
2	37946	10	1	363	10.0	9	36	7300	4.6
3	33142	10	25	6171	4.6	11	14	4176	4.9
4	44668	12	2	845	10.0	10	19	4719	6.3
5	26846	8	5	891	7.8	8	10	1701	7.0
6	35228	10	27	6655	3.9	11	10	3024	5.0
7	30520	9	34	6900	5.5	11	10	3024	7.7
8	20588	8	34	5589	6.0	7	41	5312	6.2
9	27998	9	22	4500	3.8	7	86	11072	2.3
10	35190	10	14	3509	6.4	11	10	3024	6.2
11	24588	8	24	3969	4.5	8	9	1539	5.8
12	34254	12	2	845	9.6	10	25	6171	5.0
13	36318	13	5	2156	6.9	12	2	845	7.1
Mean	31695	9.8	17.2	3715	6.5	9.4	24.5	4451	5.6
SEM	1759	0.4	3.4	652	0.6	0.5	6.1	743	0.6

RMSE root-mean-square of error, *SEM* standard error of the mean; μ and v, respectively radial and azimuthal variables, both fitted to polynomials; ψ circumferential variable, fitted to Fourier series.

Since the expanded expressions sufficiently represented the fiber angles, they were left as is without converting back to the forms of Eqs. (1) and (2). The goodness-of-fit was quantified by the root-mean-squares of the error (RMSE) computed with respect to the measured fiber angles. For reference, numerical simulations were performed using the same DTI protocols on the same diffusion tensors and amount of signal-to-noise ratio (SNR) seen in the $b0$ scans to estimate the contribution of image noise to the fiber orientation measurements.

Given that higher-order functions would necessarily yield more accurate fits, but at the same time be more sensitive to noise in the data, it was reasonable to expect there existed an optimal order that offered the best tradeoff between the two considerations. Such optimal order would correspond to the lowest order above which the fitting error stops decreasing statistically when F-tests are applied to progressively higher order functions. To this end, supposing a lower-order expression, say Model 1, had $Q1$ coefficients and corresponding fitting error of $E1$, and similarly the next

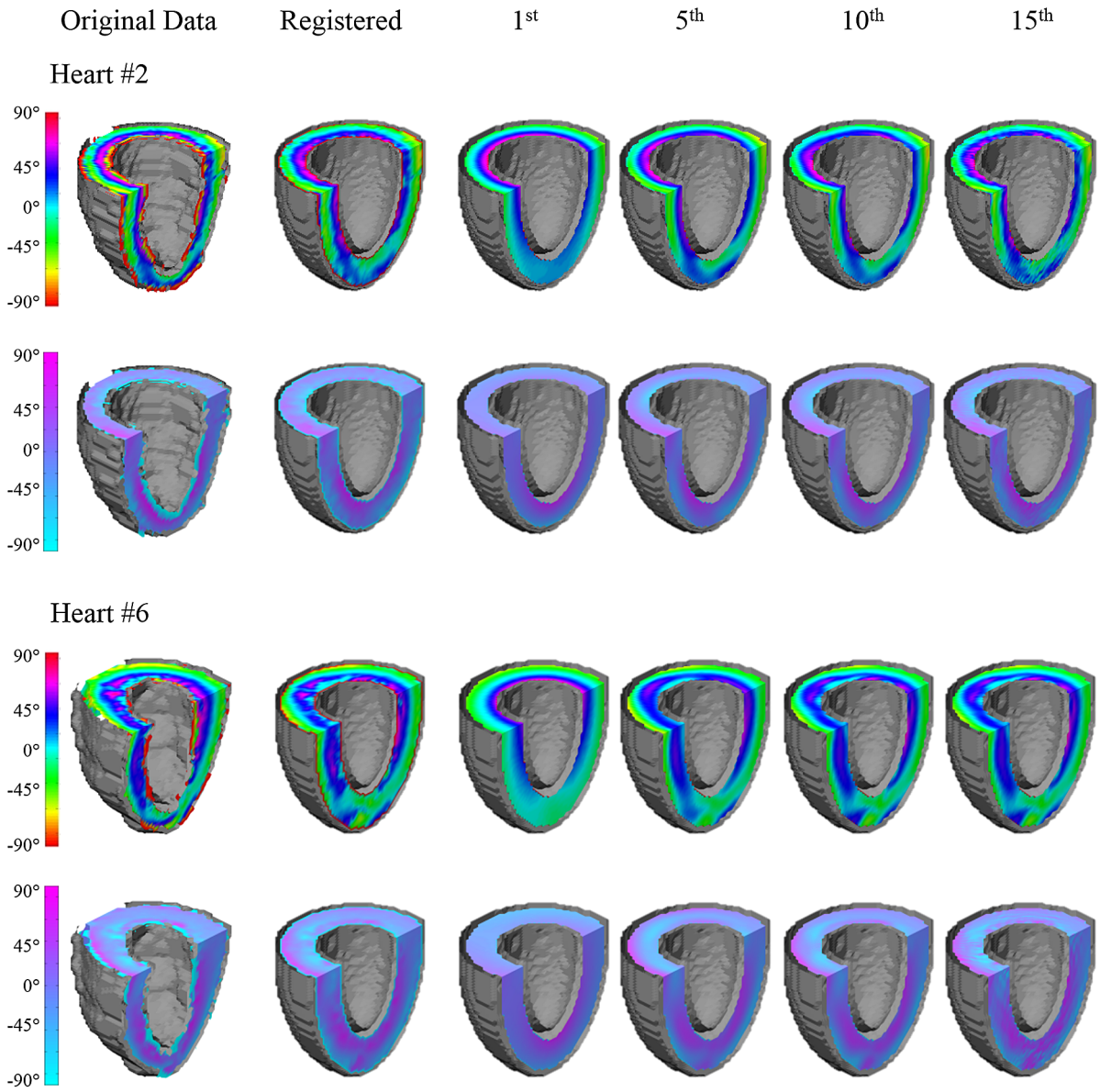

FIGURE 1. Falsecolor-coded fiber angles of two representative hearts (corresponding to #2 and #6 in Table 1). Alternate rows show helix and imbrication angle maps of the full data before and after registration to prolate spheroidal coordinates, and those fitted to the indicated order of polynomials of the radial and azimuthal prolate spheroidal variables, and Fourier series of the circumferential variable.

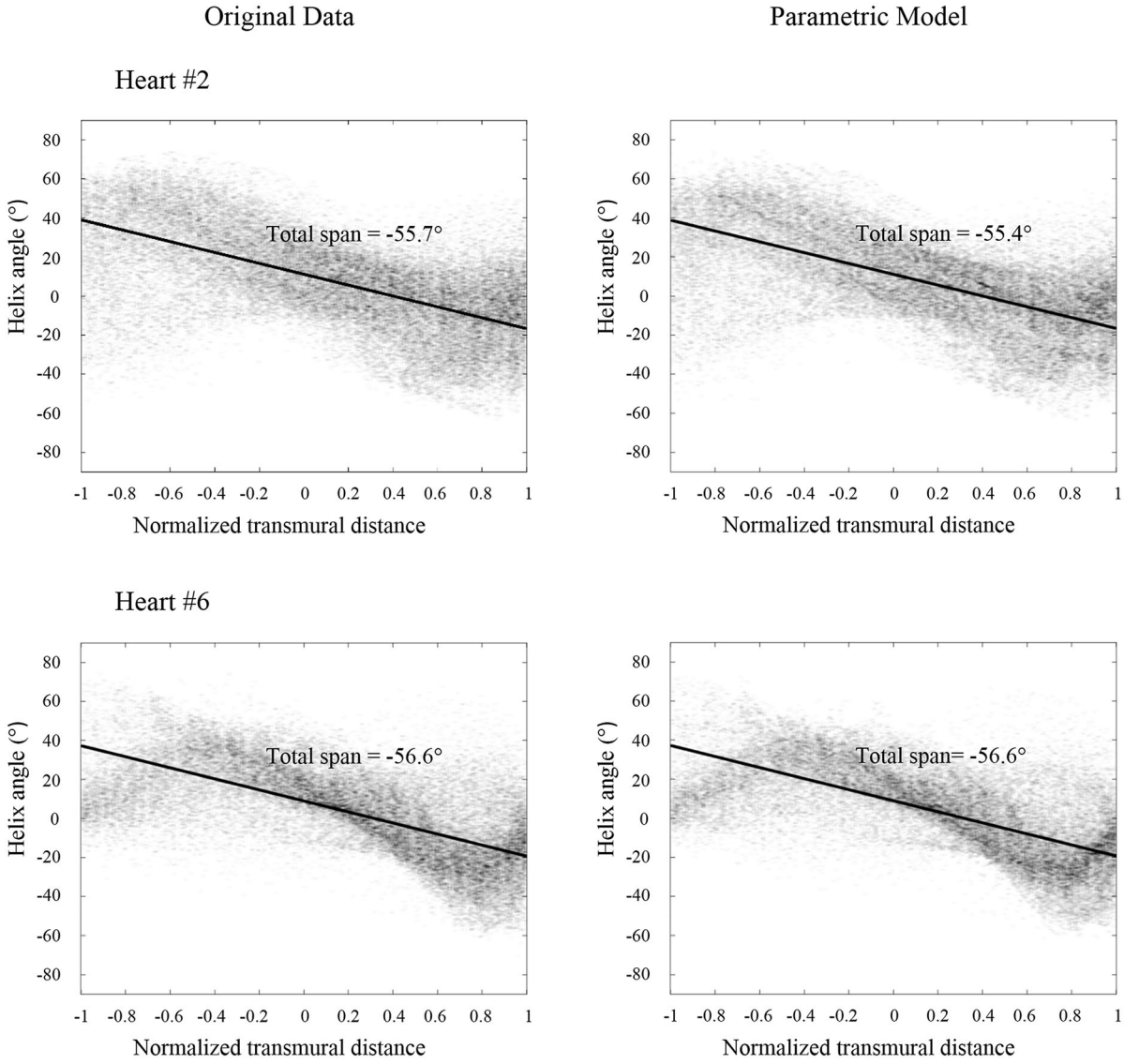

FIGURE 2. Representative scatter plots of the left ventricular myocardial fiber helix angle as function of normalized transmural distance (left direction pointing toward the epicardium). The rows show plots for different hearts obtained using original (left) and parametrically modeled (right) helix angles. Superimposed are linear regressions (solid lines) quantifying the mean total transmural span of the helix angle.

higher-order Model 2 had $Q2$ coefficients ($Q2 > Q1$) and $E2$ fitting error, the F-value for the N measurement points was calculated as,[9]

$$F = \frac{(E1 - E2)}{Q2 - Q1} \Big/ \frac{E2}{N - Q2}. \quad (7)$$

The null hypothesis, that the fitting errors in Models 1 and 2 were not statistically different, was tested by comparing the F-value to the F-distribution critical value for $(Q2 - Q1, N - Q2)$ degrees of freedom. To circumvent testing all possible permutations of the orders, F-tests were performed on the fits of α for each specimen for simultaneously increasing n_μ and n_v, while holding n_ψ constant at unity, until their optimal order was found. Subsequently, while holding n_μ and n_v constant at their optimal value, F-tests were performed for increasing n_ψ. The optimal orders of functions for the fiber imbrication angle, n'_μ, n'_ψ and n'_v, were similarly determined.

Demonstration of Utility

Due to the large dataset size of DTI experiments, computing the whole ventricle mean helix angle transmural span[11] has been commonly used to reduce and analyze the fiber orientation information. To demonstrate that the proposed polynomial representation maintained the fiber structural information they

intended to capture, a scatter plot was generated for each heart for the fiber helix angle α from the original DTI data with respect to the distance from the endocardium along all possible transmural trajectories, and the mean transmural span of the helix angle was calculated *via* linear regression. Similarly, the mean transmural span was determined for the helix angle fitted to the parametric expression with optimal orders of the constituent functions. The transmural helix angle spans quantified using the two techniques among all hearts were then compared *via* paired *t* test.

TABLE 2. Whole-LV average transmural fiber helix angle span obtained from original data and parametric models for individual hearts.

Heart#	Original (°)	Parametric (°)
1	−41.2	−41.2
2	−55.7	−55.4
3	−73.7	−73.4
4	−48.4	−47.8
5	−44.7	−45.0
6	−56.6	−56.6
7	−55.0	−54.7
8	−36.3	−36.0
9	−64.3	−64.0
10	−54.7	−54.3
11	−55.4	−55.0
12	−67.0	−66.3
13	−74.9	−74.6
Mean	−55.9	−55.7
SEM	3.1	3.1

Paired *t* test between the groups yielded $p > 0.1$.

Advances in computational anatomy have allowed the computation of digital atlases from images of the body, including the heart using DTI data.[27,30,31] To further demonstrate their practical utility, similar group atlases were constructed for the parametric models simply by (a) computing the averages of the orders of expressions deemed optimal for the individual hearts and taking them as the optimal orders for the atlas, then (b) determining the coefficients of the parametric expressions of the atlases by averaging the corresponding coefficients of the constituent hearts, since the coordinates of the representations were already standardized. To assess the goodness of the group averaged expressions, the RMS deviation of the average with respect to original (i.e., unfitted) quantities in the prolate spheroid space, as well as both voxel-based average and standard deviation of the latter, were computed.

As a final demonstration of practical utility, the parametric models were used to predict the 3D myocardial fiber structure from sub-sampled DTI datasets mimicking partial imaging of the heart to reduce

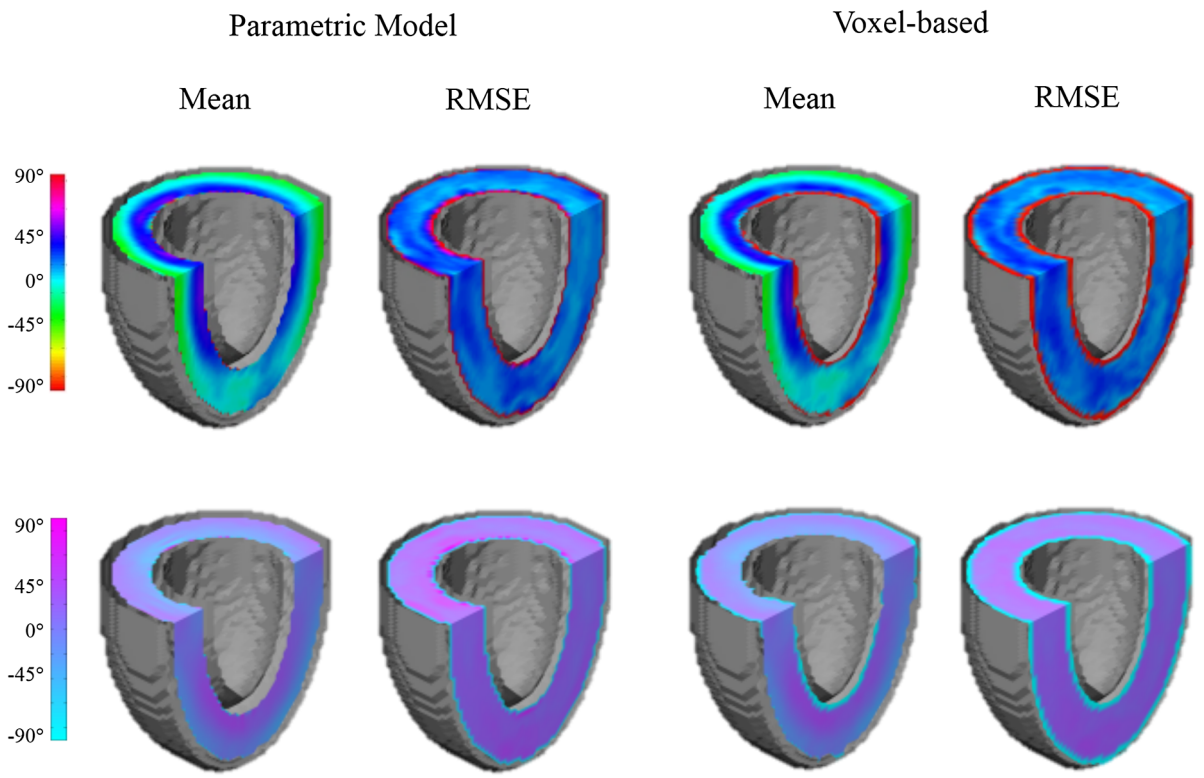

FIGURE 3. Falsecolor-coded atlases of fiber helix and imbrication angles. Maps of the group mean and corresponding RMSE (i.e., standard deviation) for both the fiber helix (top row) and imbrication angle (bottom row) constructed using parametric models (left) are highly similar to their counterparts obtained *via* voxel-based statistics (right).

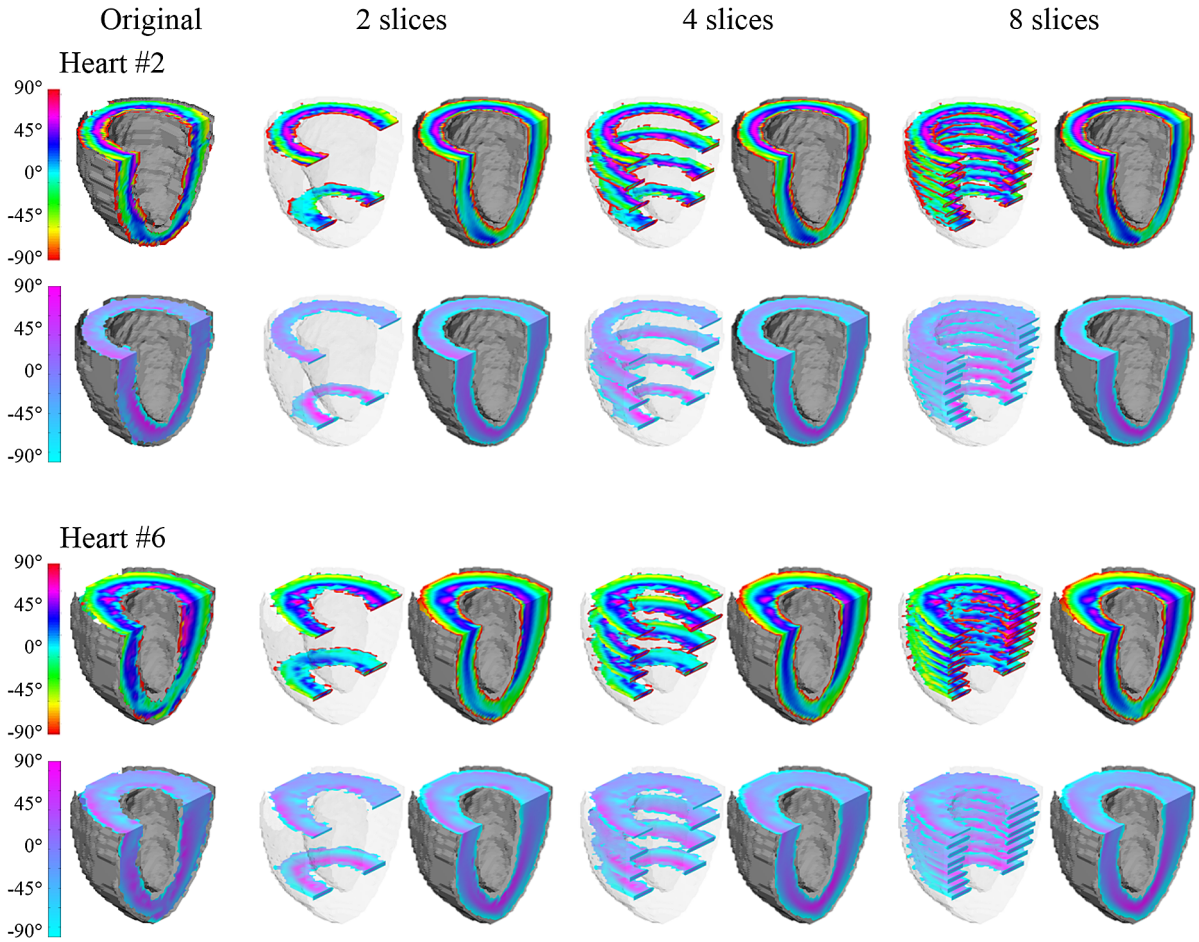

FIGURE 4. Input data and parametric model-predicted 3D fiber angles obtained for representative hearts. Alternate rows show fiber helix and imbrication angles, and each column pair corresponds to when the indicated number of slices is used as input. The left-most column contains original fiber angle data displayed in anatomical (i.e., unregistered) coordinates. The accuracy of the predictions of the helix and imbrication angles are separately tabulated in Tables 3 and 4, respectively.

TABLE 3. Root-mean-squares errors compared to the original 3D measurements of the LV myocardial fiber *helix* angles predicted by parametric models based on the indicated sub-sampling schemes, and by the group atlas.

Heart#	2 slices	4 slices	8 slices	Atlas
1	25.8	18.6	13.9	26.3
2	23.9	15.6	11.9	15.6
3	27.4	15.9	13.5	22.6
4	24.9	17.3	13.3	18.4
5	27.2	18.3	14.4	22.3
6	28.1	13.6	10.7	15.3
7	27.7	18.9	15.2	23.6
8	38.8	27.3	17.5	22.9
9	24.2	17.3	12.5	17.4
10	32.2	19.6	15.9	27.8
11	23.3	20.6	13.2	20.5
12	30.0	16.4	13.6	18.2
13	25.2	14.7	11.8	18.0
Mean	27.6*	18.0	13.6*	20.7
SEM	1.1	0.9	0.5	1.1

All entries have units of degrees.
Asterisks indicate significant column means against the atlas column *via* Bonferroni-corrected *post hoc* tests of single-factor repeated measures ANOVA with overall $p < 0.01$ significance level.

TABLE 4. Root-mean-squares errors compared to the original 3D measurements of the LV myocardial fiber *imbrication* angles predicted by parametric models based on the indicated sub-sampling schemes, and by the group atlas.

Heart#	2 slices	4 slices	8 slices	Atlas
1	24.7	20.9	15.0	23.8
2	26.0	18.8	12.8	14.3
3	27.1	19.2	15.9	20.8
4	24.2	17.6	13.5	19.2
5	33.1	18.6	13.9	18.9
6	26.8	16.3	12.8	16.3
7	33.5	22.0	16.5	21.4
8	54.0	39.9	17.9	26.3
9	25.4	18.3	13.0	18.4
10	37.4	23.0	18.9	24.3
11	24.7	23.4	16.3	21.5
12	29.1	20.1	15.3	16.7
13	31.6	18.4	14.3	17.4
Mean	30.6*	21.3	15.1*	20.0
SEM	2.2	1.6	0.5	0.9

All entries have units of degrees.
Asterisks indicate significant column means against the atlas column *via* Bonferroni-corrected *post hoc* tests of single-factor repeated measures ANOVA with overall $p < 0.01$ significance level.

the acquisition time. To this end, 2, 4 and 8 equally spaced short-axis slices of the original DTI data, spanning and including the equatorial slice and 75% of the way toward the apex, were extracted from each heart. Assuming that an anatomical scan of the ventricular morphology was available as part of the experiment, the reduced datasets were transformed into the prolate spheroidal system, and used to solve for the coefficients of the expressions describing the fiber orientation angles. Since the individual 3D DTI scans were not part of the simulated experiments, determination of the optimal orders of individual parametric models would not have been possible. Therefore, functions of the group means of optimal orders in μ and ψ were used, but to avoid creating an under-determined problem, the order for v, which was the dimension of data under-sampling, was kept at unity. Subsequently, the fitted polynomials were used to determine the fiber orientation quantities spanning the entire 3D prolate hemispheroid, which was then mapped back to the original morphology of the LV. Using the 3D DTI as gold standard, accuracy of the predicted fiber orientation quantities was determined by computing their RMSE. Finally, the RMSEs obtained for the 2, 4 and 8-slice simulations, along with the deviation obtained when the group atlas was used for the prediction and as control, were compared *via* repeated measures ANOVA.

RESULTS

The process of parametric modeling of the myocardial fiber helix and imbrication angles is visualized in Fig. 1, which shows the original fiber angles in both anatomical and prolate spheroidal coordinates, and those fitted using 1st, 5th, 10th and 15th order functions in all dimensions, obtained in two representative specimens. Excluding segmentation, representing the fiber orientation quantities in the standardized prolate spheroidal coordinates took approximately 3 min computation time, and depending on the order of the functions involved, calculation of the parametric coefficients took 3 s to 30 min.

In Fig. 1, while most of the gross structural pattern is already visible in even the 1st-order models, as expected, more details are captured in higher order representations. Notably, little difference is detectable between the 10th and 15th-order models, suggesting that, if the *F*-tests described above were performed correctly, the optimal orders for the parametric expressions should be similar. Results of the *F*-tests for the individual hearts are summarized in Table 1. On average, the optimal orders for the parametric expressions for the helix angle were found to be 10 for the polynomials and 17 for the Fourier series, and 10 and 24 for the imbrication angle, both in agreement with visual inspection of Fig. 1. Compared to 31,695 measurement points needed in voxel-based representation of the volume, the optimal-order parametric models of the helix and imbrication angles, in expanded forms, consisted of 3715 and 4451 terms, and achieved RMSE-estimated accuracies of 6.5° and 5.6°, respectively. Simulations of the same DTI experiment using the same diffusion tensor eigenvalues (1.20, 0.75 and 0.40×10^{-3} mm^2/s) and SNR (35) for the $b0$ intensity indicated that image noise accounted for 2.3° error in the fiber orientation measurements.

Figure 2 shows the scatter plots of the fiber helix angles as a function of normalized transmural distance for the same two hearts, revealing highly similar distributions between the original and parametrically modeled data. The transmural helix angle spans, obtained by linear regression of the scatter plots, for all hearts are listed in Table 2, which shows that the commonly used description of LV myocardial fiber structure determined from the parametric models is essentially identical to that in the original data.

The utility of the proposed parametric modeling approach for group analysis is demonstrated in Fig. 3, which includes the group atlases and RMSE maps computed for the parametrically represented fiber helix and imbrication angles, and those computed *via* voxel-based analysis. Both the atlases and the measures of variability appear highly similar. Quantitatively, the atlases obtained using the two approaches have a mean difference of $-0.03°$ and $-0.10°$ for the helix and imbrication angles, respectively. Moreover, the whole-volume mean RMSEs of the angles, 20.7° and 20.0° for the parametric model atlas, are highly similar to 19.6° and 18.7° calculated for the voxel-based atlases. These findings indicate that parametric modeling of myocardial fiber structure does not introduce significant systematic bias to the descriptive statistics of the group. Taking the group RMSEs as the population standard deviations, the cohort sizes necessary to make the uncertainties (i.e., standard errors) of the atlases comparable to the mean fitting errors of the individual hearts (e.g., 6.5° for α) were determined to be 10 and 13 for the fiber helix and imbrication angles, respectively.

Lastly, Fig. 4 visually describes subject-specific parametric model-based predictions of the 3D fiber structure from limited 2D data for the same two hearts shown in Fig. 1. Compared to the predictions based on 2 slices, improvements can be clearly seen when 4 or more slices are used. The RMSEs of the predictions, along with those of the parametric model and group atlas as basis of comparison, for the helix and imbrication angles for individual hearts are listed in Tables 3 and 4, respectively. Not unexpectedly, considering the ~6° mean error of the full 3D parametric models, predictions from both limited number of slices and group atlas introduce additional discrepancy in the fiber angles. Repeated measures ANOVA indicates that using 2 slices achieved worse, whereas using 4 slices yielded comparable accuracy as atlas-based predictions. Remarkably, parametric models constructed from 8 subject-specific slices predicted the 3D fiber structure significantly better than the group atlases.

DISCUSSION

Overall, results of the present study are highly promising for representing the myocardial structure, at least in the LV, based on parametric functions of the spatial variables. Using on average 10th-order polynomials in the radial and longitudinal axes, and 17th and 24th-order Fourier series for the circumferential dimension, fiber helix and imbrication angles of the individual hearts were described to 6.5° and 5.6° accuracies, respectively. Because image noise contributed to an estimated 2.3° error in the original DTI measurements, the true accuracy of the parametric representations is likely better. The parametric expressions, in expanded forms, entail 1,000 s of terms, which is about an order-of-magnitude reduction compared to the 10,000 s measurement points needed to describe the same fiber structure using voxel-based representation in the same volume. Although it remains to be determined whether the expanded representations can be reduced to the forms of Eqs. (1) and (2), and whether such feat can bring about additional advantages, the benefits of parametric modeling of myocardial structures are already clear.

Results in Figs. 2 and 3, and Table 2, demonstrate the practical utility of the proposed approach for capturing the overall transmural helix angle span and group statistics of the fiber orientation among hearts. They indicate that the conciseness of the parametric representation is achieved without introducing significant error to the descriptive information conventionally derived and used for analyzing the 3D fiber orientation measurements. Importantly, for the group analysis, the RMSEs of the parametric models provide a convenient metric of goodness for the atlases, which has been difficult to determine since the atlases exist only computationally. For the current study, a cohort size of 10–13 is what it takes to obtain an atlas of myocardial fiber orientation that has the same uncertainty as the average error in individual parametric models. While atlases have been constructed for cardiac DTI studies,[27,30,31] to the authors' knowledge, this is the first time a measure of accuracy with practical relevance is related to the cohort size and attached to an atlas.

A major advantage of the proposed parametric approach is the ability to perform subject-specific extrapolation or prediction of the 3D myocardial fiber structure from limited measurements (e.g., few 2D slices), as demonstrated in Fig. 4 and Tables 3 and 4. Given that enough slices are used (8 in the current study), fiber angles in the whole LV that are more accurate than the group atlas can be can predicted, without having to scan all hearts and construct the

group atlas. Convolution-based procedures for interpolating and extrapolating the local fiber orientation have been recently described.[38] However, without 3D DTI scans as references for comparison, the accuracy of the approach and whether it can be used for the whole 3D LV volume remain to be determined. Practical applications of DTI have been hampered by long scan times, and methodologies to accelerate the data acquisition, *via* for example compressed sensing[11,28,40] and simultaneous multi-slice acquisition,[12,26] are being actively investigated. The unique ability of parametric modeling to perform subject-specific prediction from limited acquired data makes it an excellent alternative or adjunct means to extend the 3D coverage of these acquisition-based accelerations.

As a first investigation of its kind, the current study focuses on the feasibility and demonstration of practical utility of parametric modeling of the LV myocardial fiber structure, with little or no specific effort spent on optimizing the technical procedures involved. While they do not detract from the general validity of the proposed parametric modeling approach, possible areas that can be improved include, and are not limited to (a) using orthogonal polynomials such as Chebyshev polynomials, instead of simple polynomials, in the parametric representation, which may offer more accurate modeling with fewer required terms, (b) finding better strategies for determining the optimal orders of the parametric expressions to ensure that the results represent truly optimal values, (c) using a more directly modeling the measurements as single vectors rather than paired scalar projection angles, since myocardial fiber orientation is a single entity, (d) better yet, directly modeling all underlying microstructure information as tensor quantities, and (e) extending the modeling beyond the LV fiber structure, to the myocardial sheet structure, and to both ventricles of the heart. Each of these areas represents a worthy topic for future investigations.

CONCLUSIONS

Prompted by the existence of conspicuous structural organization in the ventricular myocardium, the current study explored modeling the 3D LV fiber orientation in mouse hearts fixed at end-diastole using expressions constructed from finite orders of prolate spheroidal spatial variables. Representations of the fiber angles that were both concise and highly accurate were found, without compromising the metrics commonly obtained to assess the overall myocardial structure. While several technical aspects of the study can be enhanced, the findings underscore the general validity of the parametric approach, and are expected to have significant practical implications for characterization and modeling of the myocardial structure in the mouse and beyond.

APPENDIX

Representations of the Standardized Prolate Spheroidal LV Geometry

Based on the general equation of an upright prolate spheroidal surface with longitudinal radius a and transverse radius b in Cartesian coordinates,

$$\frac{x^2+y^2}{b^2}+\frac{z^2}{a^2}=1, \tag{8}$$

as depicted in Fig. 5, the geometry of the LV was approximated by a constant-thickness volume consisting of concentric prolate spheroidal shells specified by,

$$\frac{x^2+y^2}{(b_1-\tau w)^2}+\frac{z^2}{(a_1-\tau w)^2}=1, \tag{9}$$

where $\tau \in [0, 1]$ was the transmural distance variable, a_1 and b_1 were the outer longitudinal and transverse radii, a_2 and b_2 were the inner radii, and $w = a_1 - a_2 = b_1 - b_2$ was the wall thickness of the volume.

The Cartesian coordinates of a prolate spheroid could be alternatively represented using the spherical radial μ, circumferential ψ and azimuthal v coordinate variables and focal distance ρ according to :[3]

$$x = \rho \sinh(\mu)\sin(v)\cos(\psi) \tag{10}$$

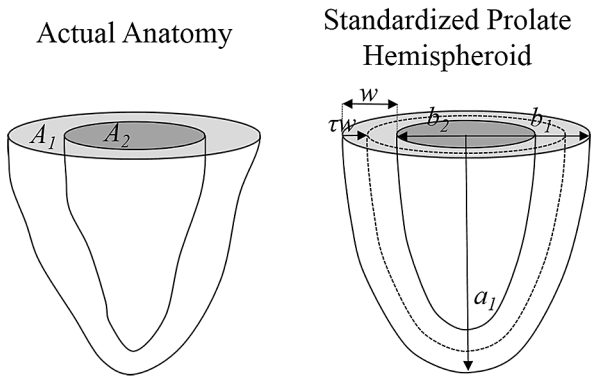

FIGURE 5. Approximation of the LV by an approximate prolate hemispheroidal volume in Cartesian coordinates. Dimensions in the anatomical space (left), including the areas of the LV in the equatorial short-axis plane and its distance to the apex, were used to compute the transverse and longitudinal axis lengths of the prolate hemispheroid (right) as specified by Eq. (9). The area A_1 included the ventricular cavity.

$$y = \rho \sinh(\mu) \sin(v) \sin(\psi) \tag{11}$$

$$z = \rho \cosh(\mu) \cos(v) \tag{12}$$

Using trigonometric manipulation, the above 3 equations were combined and reduced to

$$\frac{x^2 + y^2}{(\rho \sinh(\mu))^2} + \frac{z^2}{(\rho \cosh(\mu))^2} = \cos^2(v) + \sin^2(v) = 1. \tag{13}$$

By comparing Eq. (13) to Eq. (9), the spherical coordinates of all points in the above prolate spheroidal LV volume were found by first determining μ and ρ according to

$$\mu = \tanh^{-1}\left(\frac{b_1 - \tau w}{a_1 - \tau w}\right), \text{ and} \tag{14}$$

$$\rho = \sqrt{(a_1 - \tau w)^2 - (b_1 - \tau w)^2} = \frac{a_1 - \tau w}{\cosh(\mu)} \tag{15}$$

followed by ψ and v through

$$\psi = \tan^{-1}\frac{y}{x}, \text{ and} \tag{16}$$

$$v = \cos^{-1}\left(\frac{z}{\rho \cosh(\mu)}\right). \tag{17}$$

In the spherical coordinate system, the local tangential basis vectors, $\hat{c}$, $\hat{l}$ and $\hat{n}$ in the circumferential, longitudinal and normal (or radial) directions, respectively, were then computed according to

$$\hat{c} = \begin{bmatrix} -\sin(\psi) \\ \cos(\psi) \\ 0 \end{bmatrix}, \tag{18}$$

$$\hat{l} = \frac{-1}{\sqrt{\sinh^2(\mu) + \sin^2(v)}} \begin{bmatrix} \sinh(\mu)\cos(v)\cos(\psi) \\ \sinh(\mu)\cos(v)\sin(\psi) \\ -\cosh(\mu)\sin(v) \end{bmatrix}, \tag{19}$$

$$\hat{n} = \hat{l} \times \hat{c}. \tag{20}$$

Mapping of the Standardized Geometry to Specimen-Specific Anatomy

The standardized prolate spheroidal volume was mapped to the specimen-specific anatomy by first determining the size-related parameters in Eq. (9). As also shown in Fig. 5, since the entire transverse axis radii lay in the equatorial plane, b_1 and b_2 were respectively estimated from the areas A_1 of the LV (with filled cavity) and A_2 of its cavity in the mid-ventricular cardiac short-axis slice, according to,

$$b_1 = \sqrt{A_1/\pi}, \text{ and,} \tag{21}$$

$$b_2 = \sqrt{A_2/\pi}. \tag{22}$$

The wall thickness w was computed from $w = b_1 - b_2$. The distance from the equatorial slice to the cardiac apex was taken to be the outer longitudinal axis length a_1.

Since the prolate spheroidal shape was only an approximation of the actual LV anatomy, a one-to-one and invertible mapping between the two was obtained by registering the former to the latter *via* diffeomorphic demons.[39] For computing the local myocardial fiber orientation quantities (e.g., the helix angle) while ensuring orthogonality of the reference axes, the rotational component of the diffeomorphic transformation was used to map[2] the tangential basis vectors, $\hat{c}$, $\hat{l}$ and $\hat{n}$, for each point in the prolate spheroidal volume onto the anatomical space.

Finally, to account for size variability among hearts and facilitate numerical modeling as polynomials, the radial coordinate variable (μ, originally spanning $[\tanh^{-1}(b_1/a_1), \tanh^{-1}(b_2/a_2)]$) and azimuthal variable (v, spanning $[0, \pi]$) were both normalized *via* linear transformation to span the interval $[-1, 1]$.

ACKNOWLEDGEMENTS

The authors would like to thank Brian Watson for laboratory assistance, and Osama Abdullah and Dr. S. Joshi for their technical discussion. This work was supported by National Institutes of Health (NIH) Grants R01 HL092055 and S10 RR023017.

REFERENCES

[1]Abdullah, O. M., S. G. Drakos, N. A. Diakos, O. Wever-Pinzon, A. G. Kfoury, J. Stehlik, C. H. Selzman, B. B. Reid, K. Brunisholz, D. R. Verma, C. Myrick, F. B. Sachse, D. Y. Li, and E. W. Hsu. Characterization of diffuse fibrosis in the failing human heart via diffusion tensor imaging and quantitative histological validation. *NMR Biomed.* 27(11):1378–1386, 2014.

[2]Alexander, D. C., C. Pierpaoli, P. J. Basser, and J. C. Gee. Spatial transformations of diffusion tensor magnetic resonance images. *IEEE Trans. Med. Imaging* 20(11):1131–1139, 2001.

[3]Arfken, G. "Prolate Spheroidal Coordinates", in Mathematical Methods for Physicists (2nd ed.). Orlando: Academic Press, pp. 103–107, 1970.

[4]Arts, T., P. Bovendeerd, T. Delhaas, and F. Prinzen. Modeling the relation between cardiac pump function and myofiber mechanics. *J. Biomech.* 36(5):731–736, 2003.
[5]Basser, P. J., J. Mattiello, and D. LeBihan. MR diffusion tensor spectroscopy and imaging. *Biophys. J.* 66(1):259–267, 1994.
[6]Bayer, J. D., R. C. Blake, G. Plank, and N. A. Trayanova. A novel rule-based algorithm for assigning myocardial fiber orientation to computational heart models. *Ann. Biomed. Eng.* 40(10):2243–2254, 2012.
[7]Borgdorff, M. A. J., B. Bartelds, M. G. Dickinson, P. Steendijk, M. de Vroomen, and R. M. F. Berger. Distinct loading conditions reveal various patterns of right ventricular adaptation. *Am. J. Physiol. Heart Circ. Physiol.* 305(3):H354–H364, 2013.
[8]Bovendeerd, P. H., T. Arts, J. M. Huyghe, D. H. van Campen, and R. S. Reneman. Dependence of local left ventricular wall mechanics on myocardial fiber orientation: a model study. *J. Biomech.* 25(10):1129–1140, 1992.
[9]Brook, R. J., and G. C. Arnold. Applied Regression Analysis and Experimental Design. New York: Marcel Dekke, 1985.
[10]Chen, J., S.-K. Song, W. Liu, M. McLean, J. S. Allen, J. Tan, S. A. Wickline, and X. Yu. Remodeling of cardiac fiber structure after infarction in rats quantified with diffusion tensor MRI. *Am. J. Physiol. Heart Circ. Physiol.* 285(3):946–954, 2003.
[11]Donoho, D. L. Compressed sensing. *IEEE Trans. Inf. Theory* 52(4):1289–1306, 2006.
[12]Feinberg, D. A., and K. Setsompop. Ultra-fast MRI of the human brain with simultaneous multi-slice imaging. *J. Magn. Reson.* 229:90–100, 2013.
[13]Gaynor, S. L., H. S. Maniar, J. B. Bloch, P. Steendijk, and M. R. Moon. Right atrial and ventricular adaptation to chronic right ventricular pressure overload. *Circulation* 112(9 Suppl):I212–I218, 2005.
[14]Geerts, L., P. Bovendeerd, K. Nicolay, and T. Arts. Characterization of the normal cardiac myofiber field in goat measured with MR-diffusion tensor imaging. *Am. J. Physiol. Heart Circ. Physiol.* 283(1):H139–H145, 2002.
[15]Giannakidis, A., D. Rohmer, A. I. Veress, and G. T. Gulberg. Diffusion. Diffusion tensor magnetic resonance imaging-derived myocardial fiber disarray in hypertensive left ventricular hypertrophy: visualization, quantification and the effect on mechanical function to cite this version, 2012.
[16]Golub, G. H., and C. Reinsch. Singular value decomposition and least squares solutions. *Numer. Math.* 14(5):403–420, 1970.
[17]Healy, L. J., Y. Jiang, and E. W. Hsu. Quantitative comparison of myocardial fiber structure between mice, rabbit, and sheep using diffusion tensor cardiovascular magnetic resonance. *J. Cardiovasc. Magn. Reson.* 13(1):74, 2011.
[18]Helm, P. A., L. Younes, M. F. Beg, D. B. Ennis, C. Leclercq, O. P. Faris, E. McVeigh, D. Kass, M. I. Miller, and R. L. Winslow. Evidence of structural remodeling in the dyssynchronous failing heart. *Circ. Res.* 98(1):125–132, 2006.
[19]Holmes, A., D. F. Scollan, and R. L. Winslow. Direct histological validation of diffusion tensor MRI in formaldehyde-fixed myocardium. *Magn. Reson. Med.* 44(1):157–161, 2000.
[20]Hsu, E. W., and S. Mori. Analytical expressions for the NMR apparent diffusion coefficients in an anisotropic system and a simplified method for determining fiber orientation. *Magn. Reson. Med.* 34(2):194–200, 1995.
[21]Hsu, E. W., A. L. Muzikant, S. A. Matulevicius, R. C. Penland, and C. S. Henriquez. Magnetic resonance myocardial fiber-orientation mapping with direct histological correlation. *Am. J. Physiol. Heart Circ. Physiol.* 274(5 Pt 2):H1627–H1634, 1998.
[22]Jiang, Y., K. Pandya, O. Smithies, and E. W. Hsu. Three-dimensional diffusion tensor microscopy of fixed mouse hearts. *Magn. Reson. Med.* 52(3):453–460, 2004.
[23]Kanai, A., and G. Salama. Optical mapping reveals that repolarization spreads anisotropically and is guided by fiber orientation in guinea pig hearts. *Circ. Res.* 77(4):784–802, 1995.
[24]Koay, C. G., L.-C. Chang, J. D. Carew, C. Pierpaoli, and P. J. Basser. A unifying theoretical and algorithmic framework for least squares methods of estimation in diffusion tensor imaging. *J. Magn. Reson.* 182(1):115–125, 2006.
[25]Kung, G. L., O. M. Ajijola, R. Tung, M. Vaseghi, J. K. Gahm, W. Zhou, A. Mahajan, A. Garfinkel, K. Shivkumar, and D. B. Ennis. Microstructural remodeling in the porcine infarct border zone measured by diffusion tensor and late gadolinium enhancement MRI. *Circulation* 126(21 Supplement):A14246, 2012.
[26]Larkman, D. J., J. V. Hajnal, A. H. Herlihy, G. A. Coutts, I. R. Young, and G. Ehnholm. Use of multicoil arrays for separation of signal from multiple slices simultaneously excited. *J. Magn. Reson. Imaging* 13(2):313–317, 2001.
[27]Lombaert, H., J.-M. Peyrat, P. Croisille, S. Rapacchi, L. Fanton, F. Cheriet, P. Clarysse, I. Magnin, H. Delingette, and N. Ayache. Human atlas of the cardiac fiber architecture: study on a healthy population. *IEEE Trans. Med. Imaging* 31(7):1436–1447, 2012.
[28]Lustig, M., D. Donoho, and J. M. Pauly. Sparse MRI: the application of compressed sensing for rapid MR imaging. *Magn. Reson. Med.* 58(6):1182–1195, 2007.
[29]Mori, S., K. Oishi, and A. V. Faria. White matter atlases based on diffusion tensor imaging. *Curr. Opin. Neurol.* 22(4):362–369, 2009.
[30]Peyrat, J.-M., M. Sermesant, X. Pennec, H. Delingette, C. Xu, E. McVeigh, and N. Ayache. Towards a statistical atlas of cardiac fiber structure. *Med. Image Comput. Comput. Assist. Interv.* 9(Pt 1):297–304, 2006.
[31]Piuze, E., H. Lombaert, J. Sporring, G. J. Strijkers, A. J. Bakermans, and K. Siddiqi. Atlases of cardiac fiber differential geometry. *Lecture Notes in Computer Science (including subseries Lecture Notes in Artificial Intelligence and Lecture Notes in Bioinformatics)*, LNCS, vol. 7945, pp. 442–449, 2013.
[32]Reese, T. G., R. M. Weisskoff, R. N. Smith, B. R. Rosen, R. E. Dinsmore, and V. J. Wedeen. Imaging myocardial fiber architecture in vivo with magnetic resonance. *Magn. Reson. Med.* 34(6):786–791, 1995.
[33]Ripplinger, C. M., W. Li, J. Hadley, J. Chen, F. Rothenberg, R. Lombardi, S. A. Wickline, A. J. Marian, and I. R. Efimov. Enhanced transmural fiber rotation and connexin 43 heterogeneity are associated with an increased upper limit of vulnerability in a transgenic rabbit model of human hypertrophic cardiomyopathy. *Circ. Res.* 101(10):1049–1057, 2007.
[34]Rohmer, D., A. Sitek, and G. T. Gullberg. Reconstruction and visualization of fiber and laminar structure in the normal human heart from ex vivo diffusion tensor mag-

netic resonance imaging. *Investig. Radiol.* 42(11):777–789, 2007.

[35]Schmitt, B., K. Fedarava, J. Falkenberg, K. Rothaus, N. K. Bodhey, C. Reischauer, S. Kozerke, B. Schnackenburg, D. Westermann, P. P. Lunkenheimer, R. H. Anderson, F. Berger, and T. Kuehne. Three-dimensional alignment of the aggregated myocytes in the normal and hypertrophic murine heart. *J. Appl. Physiol.* 107(3):921–927, 2009.

[36]Scollan, D. F., A. Holmes, R. Winslow, J. Forder, S. H. Gilbert, D. Benoist, A. P. Benson, E. White, S. F. Tanner, A. V. Holden, H. Dobrzynski, O. Bernus, A. Radjenovic, A. J. Physiol, H. Circ, E. K. Englund, C. P. Elder, Q. Xu, Z. Ding, B. M. Damon, R. Integr, C. Physiol, B. Schmitt, K. Fedarava, J. Falkenberg, K. Rothaus, N. K. Bodhey, S. Kozerke, B. Schnackenburg, D. Westermann, P. Paul, R. H. Anderson, F. Berger, and T. Kuehne. Histological validation of myocardial microstructure obtained from diffusion tensor magnetic resonance imaging. *Am. J. Physiol. Heart Circ. Physiol.* 275:H2308–H2318, 1998.

[37]Streeter, D. D., H. M. Spotnitz, D. P. Patel, J. Ross, and E. H. Sonnenblick. Fiber orientation in the canine left ventricle during diastole and systole. *Circ. Res.* 24(3):339–347, 1969.

[38]Toussaint, N., C. T. Stoeck, T. Schaeffter, S. Kozerke, M. Sermesant, and P. G. Batchelor. In vivo human cardiac fibre architecture estimation using shape-based diffusion tensor processing. *Med. Image Anal.* 17(8):1243–1255, 2013.

[39]Vercauteren, T., X. Pennec, A. Perchant, and N. Ayache. Symmetric log-domain diffeomorphic registration: a demons-based approach. *Med. Image Comput. Comput. Assist. Interv.* 11(Pt 1):754–761, 2008.

[40]Welsh, C. L., E. V. R. Dibella, G. Adluru, and E. W. Hsu. Model-based reconstruction of undersampled diffusion tensor k-space data. *Magn. Reson. Med.* 70(2):429–440, 2013.

[41]Wu, M. T., M. Y. Su, Y. L. Huang, K. R. Chiou, P. Yang, H. B. Pan, T. G. Reese, V. J. Wedeen, and W. I. Tseng. Sequential changes of myocardial microstructure in patients postmyocardial infarction by diffusion-tensor cardiac MR: correlation with left ventricular structure and function. *Circ. Cardiovasc. Imaging* 2(1):32–40, 2009.

[42]Wu, E. X., Y. Wu, J. M. Nicholls, J. Wang, S. Liao, S. Zhu, C.-P. P. Lau, and H.-F. F. Tse. MR diffusion tensor imaging study of postinfarct myocardium structural remodeling in a porcine model. *Magn. Reson. Med.* 58(4):687–695, 2007.

[43]Wu, D., J. Xu, M. T. McMahon, P. C. M. van Zijl, S. Mori, F. J. Northington, and J. Zhang. In vivo high-resolution diffusion tensor imaging of the mouse brain. *Neuroimage* 83:18–26, 2013.

[44]Zhang, L., J. Allen, L. Hu, S. D. Caruthers, S. A. Wickline, and J. Chen. Cardiomyocyte architectural plasticity in fetal, neonatal, and adult pig hearts delineated with diffusion tensor MRI.". *Am. J. Physiol. Heart Circ. Physiol.* 304(2):H246–H252, 2013.